











Auger decay of  $1s^{-1}3p^{-1}nl n'l'$  doubly excited states in Ar

M. Žitnik <sup>1,2</sup>, M. Hrast,<sup>1</sup> A. Mihelič <sup>1,2</sup>, K. Bučar <sup>1,2</sup>, J. Turnšek <sup>1,2</sup>, R. Püttner <sup>3</sup>, G. Goldsztejn,<sup>4</sup> T. Marchenko,<sup>4</sup> R. Guillemin,<sup>4</sup> L. Journal,<sup>4</sup> O. Travnikova <sup>4</sup>, I. Ismail <sup>4</sup>, M. N. Piancastelli <sup>4</sup>, M. Simon,<sup>4</sup> D. Ceolin <sup>5</sup> and M. Kavčič <sup>1,2</sup>

<sup>1</sup>Jožef Stefan Institute, Jamova cesta 39, SI-1000 Ljubljana, Slovenia

<sup>2</sup>Faculty of Mathematics and Physics, University of Ljubljana, Jadranska 31, SI-1000 Ljubljana, Slovenia

<sup>3</sup>Fachbereich Physik, Freie Universität Berlin, Arnimallee 14, D-14195 Berlin-Dahlem, Germany

<sup>4</sup>Sorbonne Université, UPMC Univ Paris 06, UMR 7614, LCPMR, 75005 Paris, France

<sup>5</sup>Synchrotron SOLEIL, L'Orme des Merisiers, Saint Aubin, BP 48, F-91192 Gif-sur-Yvette Cedex, France



(Received 17 May 2023; revised 22 September 2023; accepted 18 October 2023; published 14 November 2023)

The natural widths of atomic resonances do not broaden spectral lines of emitted particles, which makes the corresponding spectroscopies suitable for high-resolution studies of x-ray absorption. While resonant inelastic x-ray scattering (RIXS) results in a narrow-band x-ray signal which primarily depends on the charge of the emitter, the resonant Auger (RA) emission is more dispersed and promises the separation of individual atomic resonances. To disentangle the  $1s^{-1}3p^{-1}nl n'l'$  absorption spectrum in Ar, we have measured a sequence of  $KM_{23} - L_{23}^2M_{23}$  RA spectra with a high experimental resolution. Although only parts of the RA spectra were reliably isolated due to the strong overlap with the intense  $K - L^2$  Auger emission from ions, the data analysis shows contributions from separate groups of resonances to the Auger signal in greater detail compared to the previous high-resolution absorption and RIXS studies. The calculated differential cross sections are consistent with the available experimental results when the angular dependence of RA emission and the interference of absorption-emission paths through different resonances are accounted for.

DOI: [10.1103/PhysRevA.108.053113](https://doi.org/10.1103/PhysRevA.108.053113)

## I. INTRODUCTION

Photoabsorption is one of the most widely used spectroscopic techniques to unravel structural and dynamical properties of matter [1] and has been improved over time to reach higher sensitivity and resolution [2]. The method consist in measuring wavelength-dependent attenuation of light passing through the sample and relies on the Beer-Lambert law [3–6] to interpret the results in terms of a single microscopic parameter, the photoabsorption cross section.

At short wavelengths and for thick targets, the x-ray yield or Auger electron yield from the photoexcited states is often measured to reconstruct photon energy dependence of the core-hole specific absorption cross section. Due to the energy conservation, such indirect measurements of absorption bypass the lifetime broadening of photoexcited atomic resonances [7]. The spectra of resonance decay products are broadened only by the experimental resolution, which is determined by the photon probe resolution ( $\Delta_p$ ) and the spectrometer resolution ( $\Delta_s$ ), and by  $\Gamma_f$ , the natural width of the relaxed final state populated by the resonant inelastic x-ray scattering (RIXS) [8–13] or resonant Auger (RA) emission [14–18]. Since  $\Gamma_f$  is usually much smaller than  $\Gamma_i$ , the natural width of the photoexcited core-hole state, the absorption spectral features are observed with a subnatural resolution as soon as  $\Delta_s \ll \Gamma_i$ . A showcase is provided by the  $L_3 - M_5$  RIXS studies in Xe, where the  $2p_{3/2}$  hole features a 2.6 eV natural linewidth and the resonant part of the photoabsorption spectrum was reconstructed with a 0.76 eV spectral broadening [19,20]. In Ar, the spectral broadening due to decay of the  $1s$  hole is about three times smaller and the resolution

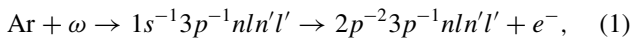
improvement of RIXS is not that dramatic [21]. However, due to the considerable shift of the  $KM_{23} - M_{23}^2$  satellite lines with respect to the diagram  $K - M_{23}$  x-ray emission line, the analysis of the experimental RIXS spectra enabled a separation of the  $1s^{-1}3p^{-1}nl n'l'$  atomic resonances and of the corresponding shake-up and shake-off continua from the predominant signal of  $1s^{-1}\epsilon p$  continuum in the absorption spectrum. In a similar way, the separation of  $1s4p$  and  $1s3d$  double excitations from the underlying  $1s$  continuum was reported for Kr [22].

While the separation of multielectronic excitations cannot be achieved by measuring attenuation of light only, the indirect two-step processes, such as RIXS and RA, do not necessarily result in the observed photon or electron yield that is proportional to the absorption spectrum. Besides the self-absorption correction, required for thick targets [23], the proportionality is broken also on an atomic level when one or more of the following conditions are met: (1) when the decay branching ratio to the observed channel varies strongly with the intermediate state [24], (2) when the atomic resonances interfere with the underlying continuum in one or more decay channels [25–27], (3) when particle emission is not isotropic and the spectrometer detects particles only within the limited solid angle, and (4) when the spectral density of intermediate states decaying to the same final state is higher than  $\Gamma_i^{-1}$  boosting the importance of the so-called lifetime interferences [28,29]. The latter effect originates in indistinguishable absorption-emission paths and is less significant for singly excited core-hole states (SESS). These states are described reasonably well by a single electronic configuration and predominantly relax with the spectator decay which en-

tures that different final states are populated even when SESs are strongly overlapping [30,31]. In the dipole approximation, the angular distribution of inelastic x-ray scattering is described by a single parameter: the asymmetry parameter  $\beta$  for a given RIXS path depends only on the total angular momenta of the initial, intermediate, and final atomic states [32]. In RA decay, the electron emission from an isolated resonance is parametrized by  $\beta$ , too, which reduces to the product of the alignment of the intermediate resonance and the anisotropy of the Auger decay. The latter is given by the sum over the electronic partial wave contributions [33].

Below we report on the  $KM_{23}-L_{23}^2M_{23}$  RA emission from the  $1s^{-1}3p^{-1}nl'n'$  doubly excited states (DESS) in argon, which complements our previous RIXS study of these states [21]. The RA emission offers the possibility to isolate contributions of different (groups of) atomic resonances to the absorption spectrum and, for the DESS, this potential has not been investigated yet. While the  $KM_{23}-M_{23}^2$  RIXS emission is delivered in the same narrow frequency window for all DESS (the satellite x-ray line), the  $KM_{23}-L_{23}^2M_{23}$  RA emission results in a characteristic combination of satellite lines covering a much wider spectral range. This rich spectral structure originates in strongly correlated multivacancy states which are involved in the transitions and causes resonance-specific arrangement of the RA yield along the electron kinetic energy axis. In comparison with RIXS, this extra dispersion of the RA signal effectively reduces overlap and promises a clearer separation of different resonant contributions in the spectral map along the photon energy axis. To interpret the results of our high resolution RA measurements, we have undertaken the multiconfiguration Dirac-Fock (MCDHF) calculations of the quantum states and of the corresponding RA transition amplitudes. The population probabilities of the  $\text{Ar}^+$  states from the atomic ground state were estimated by taking into account the interference of the RA paths through different DESS (point 4), as well as angular dependent emission of Auger electrons (point 3). The similar work we are aware of deals with SESs and reports on an angle-selective RA spectrum when the photon wavelength is tuned to the unresolved pair of the  $3d_{3/2}^{-1}5p_{3/2,1/2}$  resonances in Kr [34]. Later, the theoretical analysis was extended to include the  $3d_{5/2}^{-1}(5,6)p_{3/2}$  resonances and account for a direct photoexcitation of the  $4p^{-2}(5,6)np$  final states from the ground state of Kr to achieve closer agreement with electron angular distribution, alignment, and orientation parameters inferred from the observation of the final state fluorescence [26,28].

An attempt to reconstruct the resonant part of the absorption cross section by observing the high-energy RA electrons from the spectator decay,



necessarily fails because of the competing participator Auger decay  $1s^{-1}3p^{-1}nl'n' \rightarrow 1s^{-1} + e^-$  [27]. The induced discrete-continuum coupling is listed above under point 2 and, depending on the relative participator decay rate, it may lead to a significant rearrangement of decay branching ratios for a given resonance, invoking the consideration of point 1 too. The conversion of the photon energy dependent RA yield to the absorption is thus nonlinear and can be predicted only by expanding the theoretical analysis beyond points 3 and 4

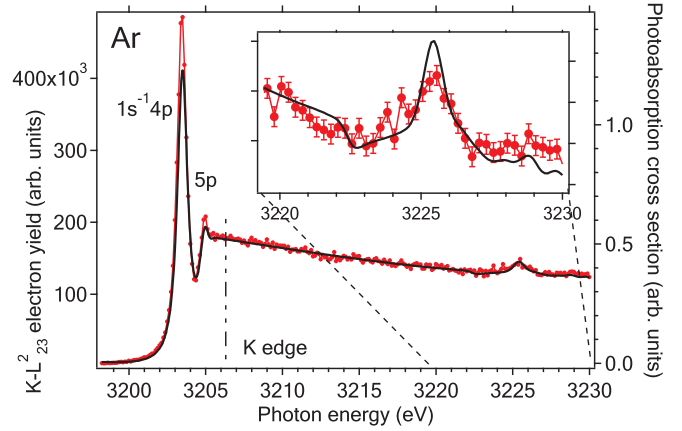


FIG. 1. Observed  $K(M)-L_{23}^2(M)$  electron yield in the vicinity of the Ar  $K$ -shell ionization threshold (red circles) together with the experimental Ar  $K$ -shell photoabsorption spectrum (black solid line). Inset: Enlarged view of the region with highest probability to photoexcite  $\text{Ar}(1s3p)^{-1}nl'n'$  resonances. To compensate for the lower resolving power, the absorption signal is scaled by a factor of 1.2 and shifted vertically to overlap the backgrounds. The Auger signal is averaged over two neighboring points of the original data set to reduce the noise level.

considered in this paper. However, the RA spectra themselves are worth studying because they contain a wealth of information about resonance positions, oscillator strengths and decay dynamics.

## II. EXPERIMENT

### A. Acquisition of experimental data

We have measured a sequence of the  $K(M_{23})-L_{23}^2(M_{23})$  Auger spectra in Ar covering a photon energy range between 3219.4 eV and 3228.0 eV with a 0.2 eV step width. The experiment was performed at the GALAXIES beamline at the SOLEIL synchrotron in France. The horizontally polarized and monochromatized light was directed through a dedicated gas target cell filled with argon. Electrons emitted in the  $45^\circ$  (0.5 sr) solid angle centered along the probe polarization axis were collected by the HAXPES Scienta R4000 hemispherical spectrometer [35].

Prior to the acquisition of the Auger spectra, the yield of  $K(M)-L_{23}^2(M)$  Auger electrons with kinetic energies in the 2635–2670 eV range was collected in the region of the Ar  $K$ -shell ionization threshold to calibrate the photon energy scale, optimize the spectrometer's collection efficiency, define the spectral window of the  $KM_{23}$  resonances, and determine the experimental resolution (Fig. 1). The spectral profile of the 3.2 keV photon beam is represented by a Gaussian with a FWHM of  $\Delta_p = 0.27$  eV, as determined from the fit of the Voigt profile to the  $1s^{-1}4p$  state in the electron spectrum (see Fig. 1) after fixing the decay width of the Ar  $K$  hole to 0.68 eV [36]. The photon energy scale was calibrated by setting the  $1s^{-1}4p$  excitation energy to 3203.54 eV [37]. In Fig. 1 the  $K(M)-L_{23}^2(M)$  Auger yield is compared to the Ar  $K$ -shell absorption spectrum. The latter was obtained from x-ray absorption measurement at the XAFS beamline of the ELETTRA synchrotron in Italy by using the photon

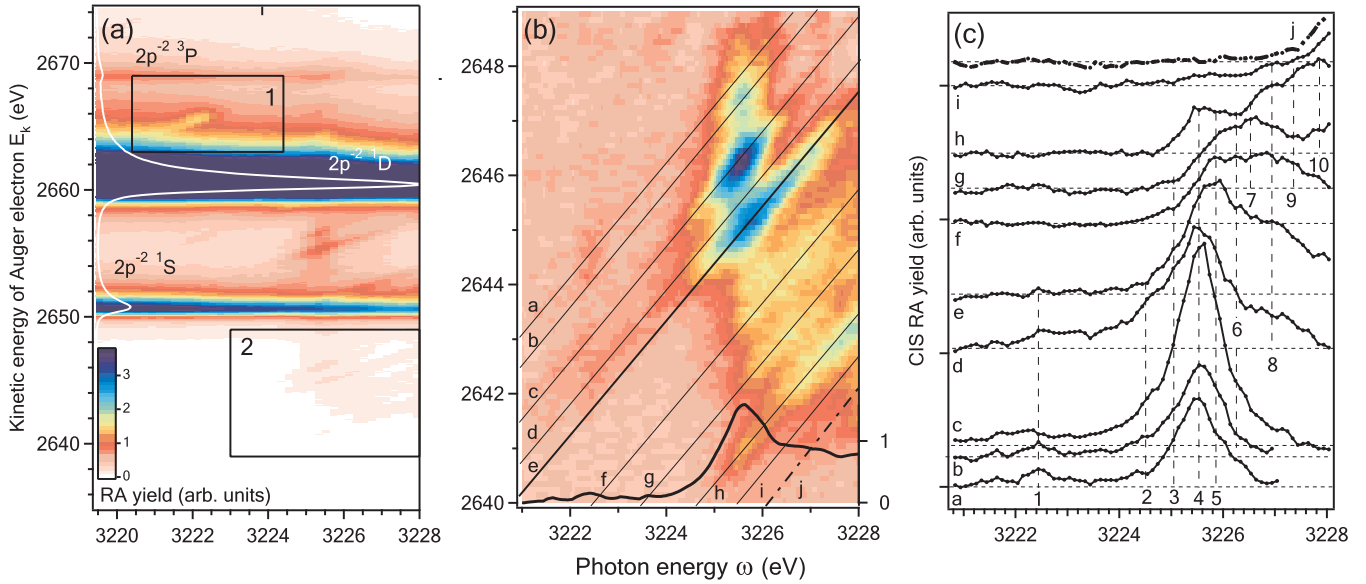


FIG. 2. (a) View of the measured  $K(M_{23})-L_{23}^2(M_{23})$  Auger map in the region of  $\text{Ar}(1s3p)^{-1}nln'l'$  DESs with the intensity (color) scale extending from zero to one-tenth of the maximum observed signal. The nonresonant  $K-L_{23}^2$  spectrum (white curve) was recorded at 3219.4 eV photon energy and is represented on the full intensity scale. Frames 1 and 2 denote areas with the dominant RA signal. (b) Full-scale view in the vicinity of frame 2 after subtraction of the  $K-L_{23}^2$  Auger signal. The projection of the RA yield on the photon energy axis is also plotted (black curve). The letters mark the final  $(2p^{-2}1S)3p^{-1}nln'l'$  states with different binding energies  $E_f$  (2). Their populations are signaled by the RA yield accumulated along  $\epsilon = \omega - E_f$  diagonals. (c) The constant ionic state (CIS) spectra reporting the RA yield to the selected final states as a function of photon energy. The peaks in the CIS spectra uncover resonance energies and are labeled by the numbered vertical dashed lines.

probe with a slightly lower resolving power. This is evident from the comparison of the signal in the SES region where the absorption shows lower contrast after normalization to the smooth part of the cross section above the threshold. Note that the modulation of the Auger yield due to the presence of the  $KM_{23}$  DESs does not strictly follow the corresponding modulation of the absorption cross section. Since the dominant nonresonant “background” of the RA signal is due to the isotropic Auger decay of the Ar  $K$  hole, the differences originate either in angle-dependent RA emission (point 3) or in the variation of the  $K-L_{23}^2$  decay branching ratios for different DESs (points 1, 2, and 4).

The spectral map in Fig. 2(a) shows a sequence of the  $K(M_{23})-L_{23}^2(M_{23})$  Auger spectra in the region of the  $1s^{-1}3p^{-1}nln'l'$  DESs. The kinetic energy resolution of the electron spectrometer at 200 eV pass energy is described by a Gaussian with a FWHM of  $\Delta_s = 0.32$  eV. This follows from the fit of the Voigt profile to the  $2p_{3/2}$  photoelectron line that was recorded at 3.2 keV photon energy using the same pass energy: the fit combines the 0.12 eV FWHM Lorentzian (describing the natural linewidth of Ar  $2p_{3/2}^{-1}$  [38]) with a Gaussian (FWHM equal to the  $(\Delta_p^2 + \Delta_s^2)^{1/2} = 0.42$  eV). The kinetic energy scale was calibrated by assigning 2660.51 eV electron kinetic energy to the maximum of the  $K-L_{23}^2$   $1D$  diagram Auger line [39].

The natural width of RA final states with two  $2p$  holes in Ar is taken to be  $\Gamma_f = 0.32$  eV [40], and the natural width of doubly excited atomic states with the  $KM_{23}$  holes is approximated by the width of the  $K$  hole. Considering the photon spectral broadening, the expected FWHM of an isolated doubly excited state in the absorption measurement

is thus 0.78 eV. Since this is larger than the expected FWHM of the same feature in the horizontal cut of the RA spectral map (0.62 eV), the cut would result in a spectrally sharper approximation of absorption trace if made at emission energy where all the resonances emit in proportion to their absorption oscillator strengths. While such cuts often exist in RIXS maps and form the basis of the so-called HERFD technique [7], in RA maps the maximum electron emission from different resonances occurs at different electron kinetic energies and the peaks are populated according to the resonance-specific branching ratios. For DESs, it is thus practically impossible to find the horizontal cut (i.e., the specific electron kinetic energy) along which the RA signal would be proportional to the resonant part of the absorption spectrum.

## B. Analysis of experimental data

In Fig. 3(a) the nonresonant Auger spectrum at 3219.4 eV photon energy is compared to the spectra taken at photon energy tuned to the lowest-lying singlet DES  $(1s3p)^{-1}4s^2 1P$  resonance at  $\omega = 3222.4$  eV, to the maximum of the  $(1s3p)^{-1}nln'l'$  RA signal at  $\omega = 3225.5$  eV and at 3.3 keV photon energy. The RA signal levels reach up to 1% of the maximum of the  $K-L_{23}^2$   $1D$  diagram line and the RA spectrum strongly overlaps with the nonresonant Auger spectrum. The intensity of the latter drops with the photon energy as dictated by the Ar  $1s$  absorption cross section and the shape of the corresponding Auger lines changes due to the postcollision interaction (PCI) [41]. This leads to large uncertainties in attempts to isolate the full RA map of the  $KM_{23}$  DESs in argon. The problem becomes manageable in the spectral

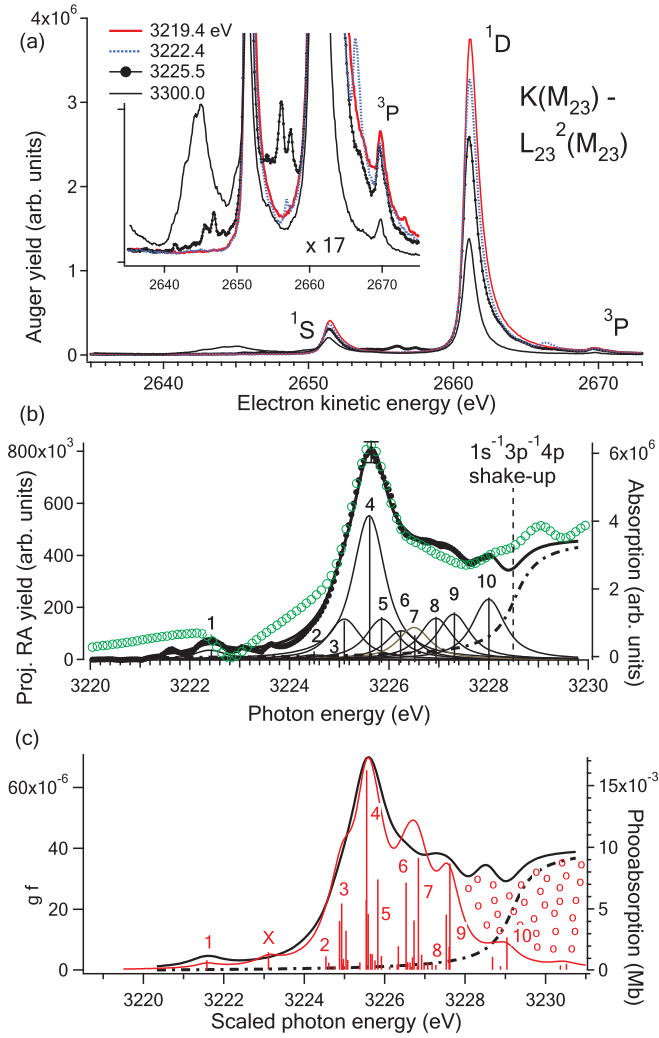


FIG. 3. (a) Comparison of the experimental  $K(M_{23})-L_{23}^2(M_{23})$  spectra in Ar: the low-energy off-resonant spectrum at 3219.4 eV photon energy (red curve), at the top of the  $1s^{-1}3p^{-1}4s^2$  resonance (3222.4 eV, blue dotted curve), at the maximum of the RA signal (3225.5 eV, black circles), and the high-energy off-resonant spectrum (3300 eV, black curve). (b) Decomposition of the RA yield in frame 2 projected on the photon energy axis (black circles) to the sum of Lorentzians (black curve) with predetermined central energies (thin black curves) and the arctan contribution of the  $1s^{-1}3p^{-1}4p$  shake-up (dash-dotted curve). A comparison with the scaled experimental absorption spectrum without the smooth background (green empty circles) is also given. (c) Comparison of the scaled fit from (b) (black curve) and the theoretical photoabsorption spectrum (red curve) constructed from the calculated  $1s^{-1}3p^{-1}nl'n'l'$  oscillator strengths  $gf$  (vertical bars). The difference (red empty circles) is attributed to the high-lying resonances and the  $1s^{-1}3p^{-1}4p$  shake-up not included in the calculation. The theoretical photon energy range is scaled by a factor of 1.2 and shifted for +0.5 eV so that the calculated positions of resonances 1 and 4 match experimental position of peaks 1 and 4, respectively. (Groups of) the calculated peaks are marked corresponding to the assignment in (b).

regions with a relatively low nonresonant Auger signal, such as the high-energy tail of the  $1^1D$  diagram line around 3222 eV photon energy [frame 1 in Fig. 2(a)] and the low-energy tail of the  $1^1S$  diagram line around 3225 eV photon energy [frame 2 in

Fig. 2(a)]. Frame 1 shows the presence of a single RA peak related to the  $1s^{-1}3p^{-1}4s^2\ ^1P \rightarrow 2p^{-2}3p^{-1}nl'n'l'(E_f) + e^-(\epsilon)$  Auger decay of the above mentioned conjugate shake-up resonance to a group of final states  $f$ , as discussed in detail in Ref. [27]. The electron signal in frame 2 [Fig. 2(b)] shows a structured emission along multiple RA paths ending mostly in the  $Ar^+(2p^{-2}\ ^1S)3p^{-1}nl'n'l'$  states along with some nonresonant emission from the  $Ar^+(1s^{-1}3p^{-1}4p)$  shake-up states [42]. The corresponding spectral map is presented in Fig. 2(b) after subtraction of the low-energy tail of the  $K-L_{23}^2\ ^1S$  diagram Auger line. The islands indicate emission from several DESs, and they are aligned in the vertical direction, indicating Auger emission from the same resonance, and diagonally, indicating Auger emission to the same final ionic state. The projection of the RA signal on the photon energy axis approximates the resonant part of the absorption cross section and enables separation of different (groups of) photoexcited resonances. However, a more precise estimation of the resonant energies can be obtained from the RA spectral map itself because the population of the final states is resonance-specific. The energy positions of active resonances were thus identified from the map in the following way: first, the final state diagonals were identified [denoted by letters in Fig. 2(b)], and then the RA yield along the diagonals was plotted as a function of photon energy [Fig. 2(c)]. Each peak in the resulting constant ionic state (CIS) spectra points to an active resonance. We have identified ten (groups of) resonances which are numbered according to their energy positions [indicated also by vertical lines in Fig. 2(c)]. This is to be compared to the four groups of resonances identified previously from the projection of the experimental RIXS map [21]. The contribution of the  $1s^{-1}3p^{-1}4p$  shake-up signal to the projection grows smoothly across the threshold at  $\omega_{su} = 3228.56$  eV [21] approximately as  $\arctan[2(\omega - \omega_{su})/\Gamma_i] + \pi/2$ , in proportion to the type  $j$  CIS spectrum in Fig. 2(c). The spectral shape and position of the shake-up signal is similar to that of the shake-off satellites which dominate the low-energy part of the  $K-L_{23}^2$  Auger spectrum at 3.3 keV photon energy [see the spectrum at  $\omega = 3300$  eV in Fig. 3(a)].

If the line shapes are known, the knowledge of peak energies significantly reduces the uncertainty of resonant contributions to the projected RA signal. A decomposition of the projection *assuming* the Lorentzian line shapes is presented in Fig. 3(b). A few lines with amplitudes comparable to the signal error bars in the 3222–3224 eV photon energy region were omitted from the analysis. The remaining ten amplitudes are just an indication of the resonance oscillator strengths as seen in the specific  $2p^{-2}\ ^1S$  decay channel. In reality, the line shapes may deviate from the Lorentzian because of the path interferences, mostly involving the neighboring DESs. Still, the set of extracted amplitudes resembles the set of calculated absorption oscillator strengths  $gf$  presented in Fig. 3(c), except for resonances 6 and 7 for which the calculations overestimate the projected yield. The calculation suggests that many more closely spaced resonances are expected to contribute to the yield meaning that the experimental RA map is not yet completely resolved. On the other hand, it is interesting to compare the projected RA signal to the resonant part of the Ar  $1s$  absorption spectrum obtained by subtraction of the smooth background determined by extrapolation of the  $\omega^{-3}$

dependence of the experimental absorption from below the resonance region [43]. The significant differences between the two spectra in Fig. 3(b) are explained by the DES coupling to the underlying  $1s^{-1}\epsilon p$  continuum via the participator Auger decay, which effectively smears out and shifts the peaks in the absorption spectrum. A good example of the strong Fano-type interference [25] is the  $1s^{-1}3p^{-1}4s^2$  resonance [number 1 in Fig. 3(b)], which is discussed in the accompanying Letter [27].

Compared to the RIXS data recorded with a similar experimental resolution, the assignment of the DES energies and their contributions to the projected RA yield is easier because the Auger electron emission is more dispersed and state-specific in comparison to x-ray emission. On the other hand, the RA spectra are more complicated and their interpretation needs a modeling support. Below we present an *ab initio* theoretical analysis of the  $KM_{23}-L^2M_{23}$  resonant Auger emission from low-lying DESs in Ar which takes into account points 3 and 4 from the Introduction.

### III. THEORY

#### A. Cross section for resonant Auger emission

In the RA process, photoionization of the ground state of atom (A) with energy  $E_g$  and angular momentum  $J_g$  (denoted by  $A|\eta_g J_g\rangle$ ) leads to the final ionic state  $A^+|\eta_f J_f\rangle$  with energy  $E_f$  and angular momentum  $J_f$  via emission of Auger electron  $e^-$  and is mediated by several intermediate (doubly excited) atomic states with energy  $E_i$  and angular momentum  $J_i$  (denoted by  $A|\eta_i J_i\rangle$ ),

$$A|\eta_g J_g\rangle + \omega(\hat{\epsilon}) \rightarrow A|\eta_i J_i\rangle \rightarrow A^+|\eta_f J_f\rangle + e^-(\mathbf{k}). \quad (2)$$

The corresponding doubly differential cross section for population of  $A^+|\eta_f J_f(E_f)\rangle$  state by emission of an electron with kinetic energy  $\epsilon = k^2/2 = \omega - E_f$  at angle  $\theta$  with respect to the light polarization axis  $\hat{\epsilon}$  is written as [44]

$$\begin{aligned} \frac{d^2\sigma_f}{d\Omega d\epsilon} &= (-1)^{J_f-J_g+\frac{1}{2}} \frac{\pi\alpha\omega}{\hat{J}_g^2} \sum_{nJ_i J_i'} \rho_{n0}^\gamma \hat{J}_i \hat{J}_i' \left\{ \begin{matrix} 1 & J_i & J_g \\ J_i' & 1 & n \end{matrix} \right\} P_n(\cos\theta) \\ &\times \sum_{lj l' j'} \hat{l} \hat{l}' \hat{j} \hat{j}' \langle l0 l'0 | n0 \rangle \left\{ \begin{matrix} l & j & \frac{1}{2} \\ j' & l' & n \end{matrix} \right\} \left\{ \begin{matrix} J_i & j & J_f \\ j' & J_i' & n \end{matrix} \right\} \\ &\times M_{lj J_i} M_{l' j' J_i'}^*, \end{aligned} \quad (3)$$

where the summation is performed over all intermediate atomic states  $A|\eta_i J_i\rangle$  visited by the transition (2). The curly and sharp brackets denote the  $6j$  symbols and Clebsch-Gordan coefficients, respectively, and  $\hat{J} \equiv \sqrt{2J+1}$ . Indices  $lj$  denote partial waves in the expansion of the emitted electron wave,  $|\chi_k\rangle = \sum_{lj} a_{lj}(\mathbf{k})|lj\rangle$ . For a long-lived final state ( $\Gamma_f \approx 0$ ), the energy conservation in reaction (1) imposes tight linear relation of electron kinetic energy with the incoming photon energy,  $\epsilon = \omega + E_g - E_f$ . The spectral broadening due to decay of the final state is accounted for by introducing the triply differential cross section  $d^3\sigma_f/(d\omega d\epsilon d\Omega)$  which equals the product of the cross section (3) and the Lorentzian factor

$$L(\epsilon; \omega + E_g - E_f, \Gamma_f) = \frac{\Gamma_f/(2\pi)}{(\epsilon - \omega - E_g + E_f)^2 + \Gamma_f^2/4}. \quad (4)$$

The matrix elements are given by

$$M_{lj J_i} = \sum_{\eta_i} \frac{\langle \eta_f J_f l j | V | \eta_i J_i \rangle \langle \eta_i J_i | D | \eta_g J_g \rangle}{\omega + E_g - E_i + i\Gamma_i/2}, \quad (5)$$

where  $V = \sum_{i>j} r_{ij}^{-1}$  is the electron transition Coulomb operator and  $D = \hat{\epsilon} \cdot \sum_i \mathbf{r}_i$  is the dipole coupling operator [34]. The amplitudes for ionization to  $\text{Ar}^+$  final ionic states with two holes in the  $L$  shell by a photon absorption directly from the atomic ground state can be neglected with respect to the resonant amplitudes in the photon energy region of the DESs. The differential RA cross section (3) is thus parametrized as

$$\frac{d^2\sigma_f}{d\Omega d\epsilon} = \pi\alpha\omega \sum_n Q_n^f(\omega) P_n(\cos\theta) \quad (6)$$

with angular weights

$$Q_n^f = \sum_{\eta_i J_i \eta_i' J_i'} \frac{A_n(\eta_i J_i, \eta_i' J_i'; \eta_f J_f) \rho_{n0}(\eta_i J_i, \eta_i' J_i'; \eta_g J_g)}{(\omega + E_g - E_i + i\Gamma_i/2)(\omega + E_g - E_i' - i\Gamma_i'/2)}. \quad (7)$$

The generalized anisotropy coefficients are expressed in terms of the reduced matrix elements of the Coulomb interaction,

$$\begin{aligned} A_n(\eta_i J_i, \eta_i' J_i'; \eta_f J_f) &= (-1)^{J_i+J_f-1/2} \hat{J}_i \hat{J}_i' \sum_{l' j'} \hat{l} \hat{l}' \hat{j} \hat{j}' \\ &\times \langle l0 l'0 | n0 \rangle \left\{ \begin{matrix} l & j & \frac{1}{2} \\ j' & l' & n \end{matrix} \right\} \left\{ \begin{matrix} J_i & j & J_f \\ j' & J_i' & n \end{matrix} \right\} \\ &\times \langle \eta_f J_f l j | V | \eta_i J_i \rangle \langle \eta_f J_f l' j' | V | \eta_i' J_i' \rangle^*. \end{aligned} \quad (8)$$

The statistical tensors of intermediate states are expressed by the reduced dipole matrix elements,

$$\begin{aligned} \rho_{n0}(\eta_i J_i, \eta_i' J_i'; \eta_g J_g) &= \frac{1}{\hat{J}_g^2} (-1)^{1+J_g+J_i} \left\{ \begin{matrix} 1 & J_i & J_g \\ J_i' & 1 & n \end{matrix} \right\} \\ &\times \rho_{n0}^\gamma \langle \eta_i J_i | D | \eta_g J_g \rangle \langle \eta_i' J_i' | D | \eta_g J_g \rangle^*. \end{aligned} \quad (9)$$

In the dipole approximation, the electron angular distribution associated with a population of a given final ionic state therefore assumes the form

$$\frac{d^2\sigma_f}{d\Omega d\omega} = \frac{1}{4\pi} \frac{d\sigma_f}{d\omega} [1 + \beta_f P_2(\cos\theta)], \quad (10)$$

where the asymmetry parameter  $\beta_f(\omega) = Q_2^f/Q_0^f$  is given by the ratio of the  $n=2$  and  $n=0$  terms in (6) and depends on the electron kinetic energy  $\epsilon$  via excitation energy of the final ionic state and the photon energy  $\omega$ . The corresponding angle-integrated differential cross section is  $d\sigma_f/d\omega = 4\pi Q_0^f(\omega)$ . For light linearly polarized along the  $z$  axis of the coordinate system, only two components of the photon statistical tensor are different from zero:  $\rho_{00}^\gamma = 1/\sqrt{3}$  and  $\rho_{20}^\gamma = -\sqrt{2/3}$ . Moreover, since the ground state of the argon atom has  $J_g = 0$ , it follows that  $J_i = J_i' = 1$  and the statistical tensors of the intermediate DESs simplify to

$$\begin{aligned} \rho_{00}(\eta_i 1, \eta_i' 1; \eta_g 0) &= \frac{1}{3\sqrt{3}} \langle \eta_i 1 | D | \eta_g 0 \rangle \langle \eta_i' 1 | D | \eta_g 0 \rangle^*, \\ \rho_{20}(\eta_i 1, \eta_i' 1; \eta_g 0) &= -\sqrt{2} \rho_{00}(\eta_i 1, \eta_i' 1; \eta_g 0). \end{aligned} \quad (11)$$

The corresponding anisotropy coefficients are then

$$A_0(\eta_i 1, \eta_i' 1; \eta_f J_f) = \sqrt{3} \sum_{lj} \langle \eta_f J_f l j || V || \eta_i 1 \rangle \langle \eta_f J_f l j || V || \eta_i' 1 \rangle^*,$$

$$A_2(\eta_i 1, \eta_i' 1; \eta_f J_f) = 3(-1)^{J_f+1/2} \sum_{l'l'j'j} \hat{l} \hat{l}' \hat{j} \hat{j}' \langle l 0 l' 0 | 20 \rangle \left\{ \begin{matrix} l & j & \frac{1}{2} \\ j' & l' & 2 \end{matrix} \right\} \left\{ \begin{matrix} 1 & j & J_f \\ j' & 1 & 2 \end{matrix} \right\} \langle \eta_f J_f l j || V || \eta_i 1 \rangle \langle \eta_f J_f l' j' || V || \eta_i' 1 \rangle^*. \quad (12)$$

Finally, the two parameters which determine the angular distribution are expressed by

$$Q_0^f(\omega) = \frac{1}{3} \sum_{lj} |M_{flj}(\omega)|^2, \quad (13)$$

$$Q_2^f(\omega) = -\sqrt{\frac{2}{3}} (-1)^{J_f+1/2} \sum_{l'l'j'j} \hat{l} \hat{l}' \hat{j} \hat{j}' \langle l 0 l' 0 | 20 \rangle \left\{ \begin{matrix} l & j & \frac{1}{2} \\ j' & l' & 2 \end{matrix} \right\} \left\{ \begin{matrix} 1 & j & J_f \\ j' & 1 & 2 \end{matrix} \right\} M_{flj}(\omega) M_{f'l'j'}^*(\omega). \quad (14)$$

In our case, the effective second-order reduced matrix element

$$M_{flj}(\omega) = \sum_{\eta_i} \frac{\langle \eta_f J_f l j || V || \eta_i 1 \rangle \langle \eta_i 1 || D || \eta_g 0 \rangle}{\omega + E_g - E_i + i\Gamma_i/2} \equiv \sum_{\eta_i} M_{flj}^{\eta_i} \quad (15)$$

depends on the photon energy and on the selected combination of the final ionic state and the partial continuum wave. It turns out that for the set of final ionic states we are dealing with, the calculations may remain limited to *s* and *d* or *p* electron waves without a considerable loss of accuracy. Then only a few *lj* combinations may contribute to the differential cross section and asymmetry parameter:

$$\frac{d\sigma_f}{d\omega} = \frac{4\pi^2\alpha\omega}{3} \left\{ |M_{f1\frac{1}{2}}|^2 + |M_{f1\frac{3}{2}}|^2, \right. \\ \left. |M_{f0\frac{1}{2}}|^2 + |M_{f2\frac{3}{2}}|^2 + |M_{f2\frac{5}{2}}|^2, \right. \quad (16)$$

$$\beta_f = \frac{8\sqrt{2}\pi^2\alpha\omega}{\sqrt{3}(d\sigma_f/d\omega)} (-1)^{J_f+1/2} \left\{ \begin{matrix} \left\{ \begin{matrix} \frac{1}{2} & \frac{3}{2} & J_f \\ \frac{1}{2} & 1 & 2 \end{matrix} \right\} |M_{f1\frac{3}{2}}|^2 - 2 \left\{ \begin{matrix} \frac{1}{2} & \frac{1}{2} & J_f \\ \frac{3}{2} & 1 & 2 \end{matrix} \right\} \text{Re}(M_{f1\frac{1}{2}} M_{f1\frac{3}{2}}^*), \\ \left\{ \begin{matrix} \frac{1}{2} & \frac{3}{2} & J_f \\ \frac{1}{2} & 1 & 2 \end{matrix} \right\} |M_{f2\frac{3}{2}}|^2 - \sqrt{\frac{12}{7}} \left\{ \begin{matrix} \frac{1}{2} & \frac{5}{2} & J_f \\ \frac{3}{2} & 1 & 2 \end{matrix} \right\} |M_{f2\frac{5}{2}}|^2 \\ - 2 \left\{ \begin{matrix} \frac{1}{2} & \frac{1}{2} & J_f \\ \frac{3}{2} & 1 & 2 \end{matrix} \right\} \text{Re}(M_{f0\frac{1}{2}} M_{f2\frac{3}{2}}^*) \\ + \sqrt{6} \left\{ \begin{matrix} \frac{1}{2} & \frac{1}{2} & J_f \\ \frac{3}{2} & 1 & 2 \end{matrix} \right\} \text{Re}(M_{f0\frac{1}{2}} M_{f2\frac{5}{2}}^*) \\ + \sqrt{\frac{12}{7}} \left\{ \begin{matrix} \frac{1}{2} & \frac{3}{2} & J_f \\ \frac{3}{2} & 1 & 2 \end{matrix} \right\} \text{Re}(M_{f2\frac{3}{2}} M_{f2\frac{5}{2}}^*) \end{matrix} \right. \quad (17)$$

The upper entry applies for final ionic states  $|\eta_f J_f\rangle$  with even parity and the lower entry for odd parity states.

### B. Effect of interferences and experimental broadening on angle-dependent RA yield

For a given final ionic state, electron emission is governed by the *lj*-specific matrix elements  $M_{flj}(\omega)$ . Depending on the photon energy and widths of the intermediate states, multiple  $g \rightarrow i \rightarrow f$  paths may significantly contribute to  $M_{flj}$  (15). When the widths are much smaller than energy separation of the neighboring DESs (the case of nonoverlapping resonances), a single path predominantly determines the  $M_{flj}$  value. In the vicinity of the *i*th resonance, the angle-integrated electron spectrum associated with final ionic state *f* is thus proportional to

$$d\sigma_f/d\epsilon = L(\omega; E_i, \Gamma_i)\sigma_f, \quad (18)$$

the product of the Lorentzian and the total RA cross section  $\sigma_f = \int d\omega(d\sigma_f/d\omega)$ . The signal pertaining to different final states unfolds along  $\epsilon = \omega + E_g - E_f$  diagonals which is a well-known characteristic of RA spectral maps presenting

the electron yield as a function of photon energy  $\omega$  and Auger electron kinetic energy  $\epsilon$ . When  $\Omega_0$ , the acceptance solid angle of the electron spectrometer is limited, the electron yield is proportional to  $K_0[\beta_f(\epsilon)]/(4\pi)(d\sigma_f/d\epsilon)$  instead. The angular acceptance scaling factor is given by

$$K_0(\beta_f) = \int_{\Omega_0} [1 + \beta_f(\omega)P_2(\cos\theta)] d\Omega. \quad (19)$$

Specifically, when the spectrometer acceptance is constant and  $\theta < \pi/8$ , the following result is obtained:

$$K_0(\beta_f) = a_0 + a_1\beta_f, \quad a_0 = 0.478, \quad a_1 = 0.425. \quad (20)$$

Note that the electron angular emission pattern does not change when the photon energy is scanned across an isolated resonance because the same energy-dependent denominator factors out from all matrix elements contributing to  $\beta_f$  (17). However, to model the weak electron emission at photon energies falling between the two well-separated resonances which decay to the same final state, the two-path interference must be considered because the corresponding amplitudes have comparable sizes there.

When the RA process involves doubly excited atomic states with a core hole, the decay widths are rather large (the case of overlapping resonances) and  $M_{flj}$  (15) may receive significant contributions from many DESs featuring nonzero reduced matrix elements with both the ground and the final state. Consequently, the single-differential cross section  $d\sigma_f/d\omega$  (or  $d^2\sigma_f/(d\omega d\epsilon)$  if  $\Gamma_f$  is not negligible), as well as  $\beta_f$  vary with photon energy in a nontrivial way. As mentioned above, an image of the RA process is often given by a two-dimensional spectral map  $J(\omega_0, \epsilon_0)$  which gives the observed Auger electron yield as a function  $\omega_0$  and  $\epsilon_0$ , the central energy of the  $T_p(\omega; \omega_0)$  spectral profile of the photon probe, and the central energy of the  $T_s(\epsilon; \epsilon_0)$  transmission function of the electron spectrometer, respectively. The calculation of the RA map starts by (1) the calculation of atomic and ionic states together with continuum waves of Auger electrons, (2) the calculation of reduced matrix elements for all paths leading from the ground to the (odd or even) final ionic state via intermediate DESs, (3) for each final state and photon energy  $\omega$ , the path amplitudes are weighted according to the photon energy detuning of the contributing intermediate states and summed over the intermediate states to generate the set of  $\omega$ -dependent matrix elements  $M_{flj}(\omega)$ , (4) matrix elements (15) are combined according to Eqs. (16) and (17) to calculate  $d\sigma_f/d\omega$  and  $\beta_f(\omega)$ , (5) each single-differential cross section is multiplied by the corresponding angular factor  $K_0[\beta_f(\omega)]/(4\pi)$  to simulate the electron yield in the limited spectrometer's acceptance angle. The electron spectrum at sharply defined photon energy  $\omega$  is obtained by (6) summing the scaled single-differential cross sections (each broadened by the Lorentzian (4) if the corresponding  $\Gamma_f$  is not negligible) over the final states, and (7) calculating the convolution of the sum  $d\sigma(\omega)/d\epsilon$  with the electron transmission function  $T_s(\epsilon; \epsilon_0)$ . Finally, the measured RA map is compared to the sequence of the RA electron spectra calculated at different central photon energies  $\omega_0$  after (8) convolving  $d\sigma(\omega)/d\epsilon_0$  with the spectral profile  $T_p(\omega; \omega_0)$ ,

$$J(\omega_0, \epsilon_0) = \int d\omega T_p(\omega; \omega_0) \left[ \int d\epsilon \left[ T_s(\epsilon; \epsilon_0) \times \sum_f K_0(\beta_f(\omega)) \frac{d\sigma_f}{d\epsilon} \right] \right]. \quad (21)$$

Of interest is also the spectral map of an effective asymmetry parameter  $\beta_{\text{eff}}$ , which describes the calculated dependence of the electron angular emission pattern on  $\omega_0$  and  $\epsilon_0$ . At each point of the map, many final channels with different  $\beta_f$  parameters contribute to the signal with different weights. The way to present the effect of the angular distribution is to evaluate the ratio of the RA yield (21) versus the RA yield calculated by setting all  $\beta_f$  to zero (isotropic emission) and equate it to the  $K_0(\beta_{\text{eff}})/K_0(0)$  ratio of angular scaling factors, defined by Eq. (20):

$$\beta_{\text{eff}}(\omega_0, \epsilon_0) = \frac{a_0}{a_1} \left( \frac{J(\omega_0, \epsilon_0)}{J(\omega_0, \epsilon_0)|_{\text{all } \beta_f=0}} - 1 \right). \quad (22)$$

In the model there is a possibility to switch off path interferences but still account for the angle-dependent emission along

each RA path. To the purpose, Eqs. (16) and (17) are modified by replacing the absolute squares and products of the effective reduced matrix elements according to

$$|M_{flj}|^2 \rightarrow \sum_{n_i} |M_{flj}^{n_i}|^2, \\ M_{flj} M_{f'l'j'}^* \rightarrow \sum_{n_i} M_{flj}^{n_i} (M_{f'l'j'}^{n_i})^*. \quad (23)$$

On the other hand, by setting the angular scaling factors to  $K_0(0) = a_0$  for all emission paths, angular dependence of the simulated spectrum is switched off so that the effects of both the interferences and angular dependent emission can be studied separately.

### C. Calculation of atomic and ionic states

The above described theoretical framework was applied to calculate  $K-L_{23}^2$  amplitudes for the Auger decay of low-lying odd-parity  $1s^{-1}3p^{-1}nl'n'l'$  photoexcited states in Ar. As noted before, the most probable decay of these states is the spectator Auger transition to  $2p^{-2}3p^{-1}nl'n'l'$  states of  $\text{Ar}^+$  where only the even parity Auger electron partial waves contribute to the RA cross section (16). The corresponding atomic and ionic bound states were calculated in the frame of the multiconfiguration Dirac-Fock method using `Grasp(92)` and `re1ci` modules of the `Ratip2012` package [45]. To describe the intermediate atomic state functions with  $J_i = 1$  in the average-level optimization scheme, 110 doubly excited configuration state functions with  $nl'n'l' \in \{4p^2, 4s^2, 3d4s, 3d^2, 4d^2, 4s4d, 3d4d\}$  were employed. The 2655 odd-parity configuration state functions within the same  $nl'n'l'$  set were selected to describe the final ionic states. The total angular momentum of these states was limited to  $J_f = 1/2, 3/2, 5/2$ , or  $7/2$  because only  $s$  and  $d$  electronic partial waves give important contributions to the Auger decay rate. The reduced dipole matrix elements between the ground state and the photoexcited intermediate states and the reduced Coulomb matrix elements between the intermediate and final continuum states were calculated using `reos` and `auger` modules, respectively, also a part of the `Ratip2012` package.

The calculation of dipole transition matrix elements requires a prior expansion of the atomic state functions in Slater determinants (provided by `cesd` module) in order to handle the nonorthogonality of the two sets of radial orbitals optimized separately for the ground state and intermediate state configurations [46]. The calculated values of transition energies and generalized oscillator strengths  $gf$  of the strongest (groups of) transitions are reported in Table I using the velocity form of the dipole matrix elements. Except for a few outliers, the length form results agree to within 10%–20%. In major part, the transition energies and oscillator strengths agree with previously published values, obtained in the non-relativistic approximation [21,47]. As described in Ref. [47], the oscillator strengths were converted to the photoabsorption spectrum and compared with the experimental data in Fig. 3. The present calculation scheme leads to a more accurate magnitude of DES photoabsorption cross section with respect to the results in Ref. [21]. To check for the consistency of the selected computational approach, we have separately calculated

TABLE I. Relative intensities of Ar  $1s^{-1}3p^{-1}nl'n'l'$  DESs, obtained by fitting the set of Lorentzians to the RA signal in frame 2 projected on the photon energy axis [see Fig. 2(b)]. Energy positions of resonances and their numbering were determined previously by inspection of the  $(2p^{-2}1S)nl'n'l'$  CIS traces [Fig. 2(c)]. The second and third columns comprise the experimental values. Correspondence with the calculated resonances is given in Fig. 3(c). Calculated energy positions are reported in the fourth column, and the generalized oscillator strengths  $gf$  in the fifth. The resonance denoted by X is only hinted in the experimental data.

Resonance number	$E_i$ (eV)	Relative intensity	$E_i$ (eV)	$gf$ ( $\times 10^{-4}$ )	Main $nl'n'l'$ configuration
1	3222.4	0.06	3221.1	0.03	$4s^2$
X			3222.6	0.06	$4s4d$
2	3224.5	0.02	3224.0	0.04	$4p^2$
3	3225.1	0.28	3224.5	0.60	$4p^2/3d4s$
4	3225.6	1.00	3225.1	1.21	$4p^2/3d4s$
5	3225.9	0.28	3225.4	0.35	$3d4s$
6	3226.2	0.18	3225.9	0.37	$4d^2/3d4s$
7	3226.5	0.22	3226.3	0.59	$3d4d/4d^2$
8	3226.9	0.29	3227.0	0.18	$3d4d$
9	3227.3	0.31	3227.1	0.43	$3d4d$
10	3228.0	0.42	3228.4	0.16	$3d4d$
Shake-up	3228.5	0.27			$4p$

oscillator strength for a dominant ground state transition to the  $1s^{-1}4p$  SES ( $gf = 0.018$ ). The calculated SES/DES ratio is reasonably close to the ratio, indicated by photoabsorption experiments (see Fig. 1 and [48]).

The experimental energy positions of Ar  $1s^{-1}3p^{-1}nl'n'l'$  DESs and their relative photo-excitation intensities are also reported in Table I. The calculated photoabsorption spectrum in Fig. 3(c) traces quite well the projection of the experimental RA map in Fig. 2(b) provided the photon energy scale is shifted for +0.5 eV (so that the maximum signal of the calculated photoabsorption occurs at the same photon energy as the maximum of the projected signal), and the calculated photon energy axis is scaled for a factor of 1.2 around that photon energy. The main configurations contributing to strongly excited (groups of) doubly excited states and their excitation energies are similar to the ones obtained previously by the nonrelativistic multiconfiguration calculation schemes (see [21] and references therein). As noted before, the dominant contribution to the absorption of DESs comes from the ground state shake-up excitation of the  $1s^{-1}3p^{-1}4p^2$  configuration state that mixes into many DES states due to electron correlations. The peak at the lowest photon energy is assigned to the conjugate shake-up excitation of the  $1s^{-1}3p^{-1}4s^2$  state [21].

To reduce the amount of numerical calculations, the  $K-L_{23}^2$  Auger matrix elements were evaluated only for 46 out of the 110 intermediate atomic states with  $gf > 10^{-6}$ . In summary, the 248 814 RA amplitudes to the 2655 final ionic states were calculated in order to build up the  $KM_{23}-L_{23}^2M_{23}$  RA map presented in Fig. 4.

#### IV. RESULTS

The results of our analysis of the experimental spectra were presented in Sec. II. Below we discuss different features of the

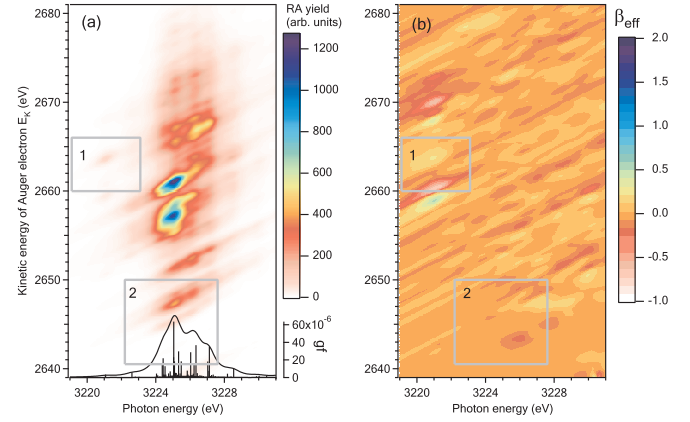


FIG. 4. (a) Calculated  $K-L_{23}^2$  RA map of the Ar  $(1s3p)^{-1}nl'n'l'$  DESs convolved with experimental widths  $\Delta_s = 0.32$  eV and  $\Delta_p = 0.27$  eV for Auger electrons emitted into a  $45^\circ$  solid angle around the polarization direction of the incoming light [see Eq. (21)]. The projection of the RA yield on the photon energy axis is plotted together with bars denoting the calculated DESs absorption oscillator strengths ( $gf$ ). (b) Map of effective asymmetry parameter  $\beta_{\text{eff}}$  defined by Eq. (22). The two annotated frames on the calculated map approximately correspond to frames 1 and 2 in Fig. 2(a).

calculated RA maps and compare them to the experimental data.

Figure 4(a) presents the calculated  $K-L_{23}^2$  RA spectral map  $J(\omega_0, \epsilon_0)$  together with its projection on the photon energy axis in the full energy range. The calculated projection is proportional to the calculated DES absorption spectrum and in principle should be close to the experimental projection unless the effects under points 1 and 2 of the Introduction are important. Calculations indicate that the majority of the RA signal overlaps with the signal of the  $K-L_{23}^2$  diagram Auger emission. In fact, frames 1 and 2 contain a relatively small amount of the RA signal but were selected for the comparison because in these spectral regions the diagram Auger signal can be reliably subtracted from the experimental data. The map of the calculated effective asymmetry parameter (22) in the full spectral range is reported in Fig. 4(b). Although the angular parameter values are limited to the  $-0.7 < \beta_{\text{eff}} < 0.5$  range, in most places  $\beta_{\text{eff}}$  is close to zero meaning that mostly isotropic RA signal is expected. This is also evident from the data calculated at the maximum of the RA signal ( $\omega = 3225.0$  eV) where  $\beta_{\text{eff}}$  varies in the  $\pm 0.2$  range [Fig. 5(a)]. We see that switching off the path interferences does not have a strong effect on the effective asymmetry parameter. However, several significant changes appear regarding the spectral shape itself and the comparison with the experimental spectrum in Fig. 5(b) shows that the RA spectrum calculated with path interferences agrees better with the measured data than the one with skipped interference terms. In Fig. 6 the theoretical results are compared with the experimental data in spectral frame 1 which contains the strongest RA emission line from the  $1s^{-1}3p^{-1}4s^2$  resonance. Evidently, the calculated RA map with an angular effect included [Fig. 6(d)] agrees better with the experimental data [Fig. 6(a)] than the angle-integrated RA yield with [Fig. 6(c)] and without considering the interferences [Fig. 6(b)]. Indeed, for such an isolated resonance,



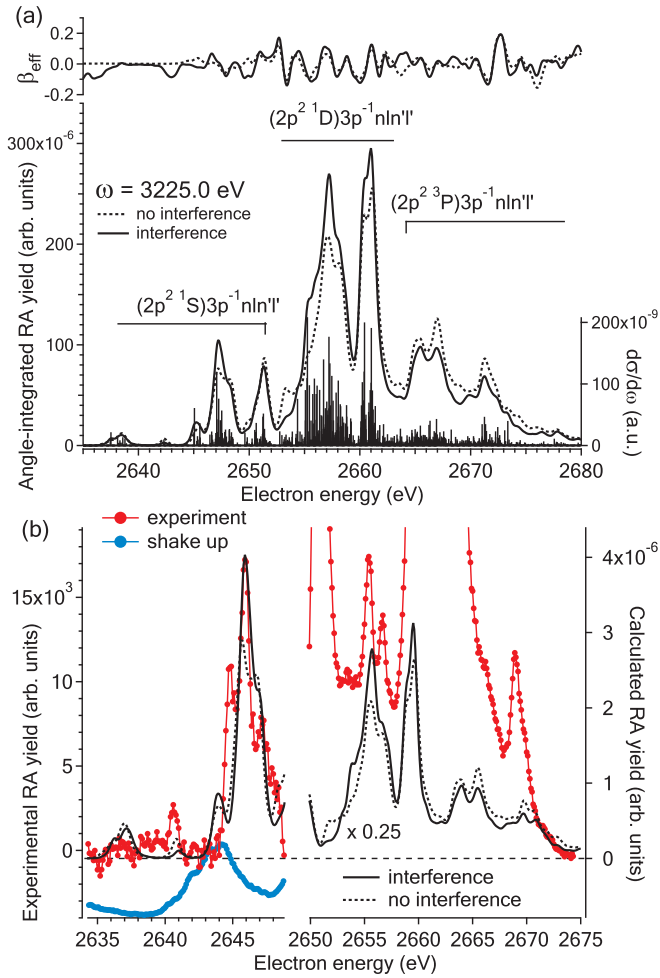


FIG. 5. (a) Calculated  $K-L_{23}^2$  RA spectrum at photon energy with the maximum calculated  $KM_{23}$  satellite photoexcitation ( $\omega = 3225.0$  eV) and the effective asymmetry parameter calculated with and without the path interference terms. The vertical bars denote probabilities to populate different  $Ar^+2p^{-2}3p^{-1}nl'n'l'$  final states. (b) Comparison with the experimental data after subtraction of the (shake-up) contribution, estimated from the measurements at 3.3 keV photon energy (blue line; see also [42]). Note that only the low-energy part of the experimental spectrum (2635–2650 eV) has the nonresonant Auger signal subtracted and that all electron spectra in the high-energy region (2650–2677 eV) are scaled by 0.25. The calculated spectrum is shifted for +0.5 eV on the experimental electron energy axis.

the difference in angular emission pattern related to different final states may have an effect on the observed RA yield but not the path interference. In fact, we see in Fig. 4(b) that  $\beta_{\text{eff}}$  approaches  $-0.7$  in the lower part of spectral frame 1. This results in the reduced Auger emission in the direction towards the electron spectrometer, in agreement with the observed disappearance of the corresponding peak. The strong asymmetry of the predominant peak in frame 1 cannot be explained within the presented theoretical frame and is discussed separately [27]. For spectral frame 2, the similar comparison is made in Fig. 7. As in the case of the RA spectrum in Fig. 5(a), angular effects are not important [compare Fig. 7(c) to Fig. 7(d)] but the inclusion of path interferences brings the

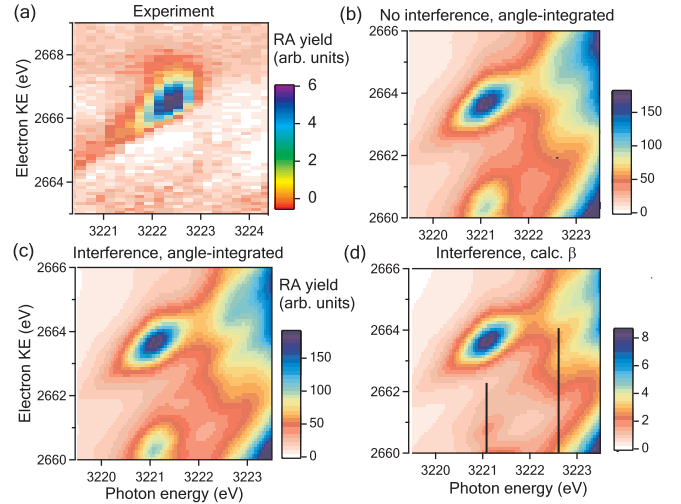


FIG. 6. Comparison of the measured (a)  $KM_{23}-L_{23}^2M_{23}$  RA map in the spectral frame 1 with the calculated RA map (b)–(d). In (d) sticks indicate calculated DES positions and relative oscillator strengths.

calculated spectral map in closer agreement with the experimental one [see also Fig. 5(b)].

V. CONCLUSIONS

We have measured the  $K-L_{23}^2$  Auger spectra in the region of photoexcited  $1s^{-1}3p^{-1}nl'n'l'$  resonances situated 15–21 eV above the Ar K-ionization threshold. Due to the strong overlap of the resonant Auger signal with the intense  $K-L_{23}^2$  signal from  $Ar^+1s^{-1}$  ions we could reliably isolate RA signal in two specific spectral frames only. The analysis of the CIS spectra extracted from spectral frame 2 enabled the identification of excitation energies for ten (groups) of resonances.

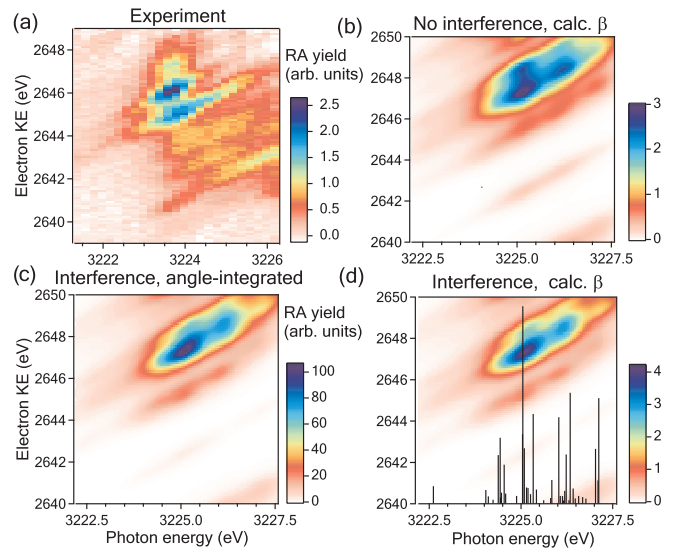


FIG. 7. Comparison of the measured (a) and calculated  $KM_{23}-L_{23}^2M_{23}$  RA maps (b)–(d) in spectral frame 2 [see Figs. 2(a) and 4] showing the relative importance of interference and angular effect on the RA electron emission. In (d), sticks indicate calculated DES positions and relative oscillator strengths.

This is significantly more than four, identified previously from the  $K-M_{23}$  RIXS measurements on the same target, and illustrates higher spectral sensitivity of the RA process at comparable experimental resolution. The RA signal in spectral frames 1 and 2 is quite well reproduced by our model calculations which account for the angular distribution of the resonant Auger emission and deal also with path interferences. Both effects improve reliability of model predictions and are necessary to consider when dealing with angle-selective detection of electrons emitted by strongly overlapping resonances. The remaining discrepancies with the experimental data are understood to originate from the omission of highly excited DESs, converging to the  $Ar^+1s^{-1}3p^{-1}nl$  shake-up threshold. Moreover, except for the case of the  $1s^{-1}3p^{-1}4s^2$  resonance described in Ref. [27], the discrete-continuum coupling is not considered. Such a coupling is promoted by the participator Auger decay of DESs and may prevent the

reconstruction of photoabsorption in the resonance region by projection of the spectator RA yield on the photon energy axis. The features presented in this paper are rather general and are likely to play the role in any future studies of the resonant Auger decay of DESs with an inner-shell vacancy.

#### ACKNOWLEDGMENTS

This work was financially supported by the Slovenian Research Agency in the framework of research program P1-0112 Studies of Atoms, Molecules and Structures by Photons and Particles. We are grateful to the SOLEIL staff for their operation of the facility. We thank the XAFS beamline staff at ELETTRA for assistance in acquiring the absorption spectrum at the  $K$  edge of argon. The authors acknowledge the HPC RIVR consortium and SLING for providing the computing resources of the HPC systems Arnes, NSC and Trdina.

- 
- [1] D. N. Sathyanarayana, *Electronic Absorption Spectroscopy and Related Techniques* (Universities Press, India, 2001).
- [2] F. Gel'mukhanov, M. Odelius, S. P. Polyutov, A. Föhlisch, and V. Kimberg, *Rev. Mod. Phys.* **93**, 035001 (2021).
- [3] P. Bouguer, *Essai D'optique Sur la Gradation de la Lumière* (Claude Jombert, Paris, 1729), pp. 16–22.
- [4] J. H. Lambert, *Photometria Sive de Mensura et Gradibus Luminis, Colorum et Umbrae (Photometry, or, On the Measure and Gradations of Light, Colors, and Shade)* (Augsburg Augusta Vindelicorum, Eberhardt Klett, 1760).
- [5] A. Beer, *Ann. Phys. (Berlin)* **162**, 78 (1852).
- [6] M. Žitnik, Š. Krušič, K. Bučar, and A. Mihelič, *Phys. Rev. A* **97**, 063424 (2018).
- [7] K. Hämäläinen, D. P. Siddons, J. B. Hastings, and L. E. Berman, *Phys. Rev. Lett.* **67**, 2850 (1991).
- [8] P. Eisenberger, P. M. Platzman, and H. Winick, *Phys. Rev. Lett.* **36**, 623 (1976).
- [9] C. F. Hague, M. Tronc, Y. Yanagida, A. Kotani, J. H. Guo, and C. Sâthe, *Phys. Rev. A* **63**, 012511 (2000).
- [10] J.-H. Guo, Y. Luo, A. Augustsson, J.-E. Rubensson, C. Sâthe, H. Ågren, H. Siegbahn, and J. Nordgren, *Phys. Rev. Lett.* **89**, 137402 (2002).
- [11] H. Hayashi, Y. Udagawa, W. A. Caliebe, and C.-C. Kao, *Phys. Rev. B* **66**, 033105 (2002).
- [12] J.-P. Rueff, L. Journel, P.-E. Petit, and F. Farges, *Phys. Rev. B* **69**, 235107 (2004).
- [13] R. G. Castillo, A. W. Hahn, B. E. Van Kuiken, J. T. Henthorn, J. McGale, and S. DeBeer, *Angew. Chem. Int. Ed.* **60**, 10112 (2021).
- [14] G. S. Brown, M. H. Chen, B. Crasemann, and G. E. Ice, *Phys. Rev. Lett.* **45**, 1937 (1980).
- [15] A. Kivimäki, A. Naves de Brito, S. Aksela, H. Aksela, O.-P. Sairanen, A. Ausmees, S. J. Osborne, L. B. Dantas, and S. Svensson, *Phys. Rev. Lett.* **71**, 4307 (1993).
- [16] R. Camilloni, M. Žitnik, C. Comicioli, K. C. Prince, M. Zaccagna, C. Crotti, C. Ottaviani, C. Quaresima, P. Perfetti, and G. Stefani, *Phys. Rev. Lett.* **77**, 2646 (1996).
- [17] P. Lablanquie, F. Penent, R. I. Hall, H. Kjeldsen, J. H. D. Eland, A. Muehleisen, P. Pelicon, Ž. Šmit, M. Žitnik, and F. Koike, *Phys. Rev. Lett.* **84**, 47 (2000).
- [18] R. Püttner, K. Jänkälä, R. K. Kushawaha, T. Marchenko, G. Goldsztejn, O. Travnikova, R. Guillemin, L. Journel, I. Ismail, B. Cunha de Miranda *et al.*, *Phys. Rev. A* **96**, 022501 (2017).
- [19] M. Žitnik, M. Kavčič, K. Bučar, A. Mihelič, M. Štuhec, J. Kokalj, and J. Szlachetko, *Phys. Rev. A* **76**, 032506 (2007).
- [20] M. Kavčič, M. Žitnik, K. Bučar, A. Mihelič, B. Marolt, J. Szlachetko, P. Glatzel, and K. Kvashnina, *Phys. Rev. B* **87**, 075106 (2013).
- [21] M. Kavčič, M. Žitnik, K. Bučar, A. Mihelič, M. Štuhec, J. Szlachetko, W. Cao, R. Alonso Mori, and P. Glatzel, *Phys. Rev. Lett.* **102**, 143001 (2009).
- [22] M. Kavčič, M. Žitnik, D. Sokaras, T.-C. Weng, R. Alonso-Mori, D. Nordlund, J.-C. Dousse, and J. Hozowska, *Phys. Rev. A* **90**, 022513 (2014).
- [23] P. Pfalzer, J.-P. Urbach, M. Klemm, S. Horn, M. L. denBoer, A. I. Frenkel, and J. P. Kirkland, *Phys. Rev. B* **60**, 9335 (1999).
- [24] M. Žitnik, M. Kavčič, K. Bučar, A. Mihelič, and R. Bohinc, *J. Phys.: Conf. Ser.* **488**, 012014 (2014).
- [25] U. Fano, *Phys. Rev.* **124**, 1866 (1961).
- [26] B. M. Lagutin, I. D. Petrov, V. L. Sukhorukov, S. Kammer, S. Mickat, R. Schill, K.-H. Schartner, A. Ehresmann, Y. A. Shutov, and H. Schmoranzer, *Phys. Rev. Lett.* **90**, 073001 (2003).
- [27] M. Žitnik, M. Hrast, A. Mihelič, K. Bučar, J. Turnšek, R. Püttner, G. Goldsztejn, T. Marchenko, R. Guillemin, L. Journel, O. Travnikova, I. Ismail, M. N. Piancastelli, M. Simon, D. Ceolin, and M. Kavčič, companion paper, *Phys. Rev. Lett.* **131**, 203001 (2023).
- [28] B. M. Lagutin, I. D. Petrov, V. L. Sukhorukov, P. V. Demekhin, B. Zimmermann, S. Mickat, S. Kammer, K.-H. Schartner, A. Ehresmann, Y. A. Shutov, and H. Schmoranzer, *J. Phys. B: At. Mol. Opt. Phys.* **36**, 3251 (2003).
- [29] M. Žitnik, M. Kavčič, R. Bohinc, K. Bučar, A. Mihelič, W. Cao, R. Guillemin, L. Journel, T. Marchenko, S. Carniato *et al.*, *J. Electron Spectrosc. Relat. Phenom.* **204**, 356 (2015).
- [30] J.-E. Rubensson, M. Neeb, A. Bringer, M. Biermann, and W. Eberhardt, *Chem. Phys. Lett.* **257**, 447 (1996).
- [31] M. Kavčič, M. Žitnik, K. Bučar, A. Mihelič, S. Carniato, L. Journel, R. Guillemin, and M. Simon, *Phys. Rev. Lett.* **105**, 113004 (2010).

- [32] M. Žitnik, K. Bučar, M. Štuhec, F. Penent, R. I. Hall, and P. Lablanquie, *Phys. Rev. A* **65**, 032520 (2002).
- [33] J. Tulkki, H. Aksela, and N. M. Kabachnik, *Phys. Rev. A* **48**, 2957 (1993).
- [34] M. Kitajima, M. Okamoto, Y. Shimizu, H. Chiba, S. Fritzsche, N. M. Kabachnik, I. P. Sazhina, F. Koike, T. Hayaishi, H. Tanaka *et al.*, *J. Phys. B: At. Mol. Opt. Phys.* **34**, 3829 (2001).
- [35] D. Céolin, J. Ablett, D. Prieur, T. Moreno, J.-P. Rueff, T. Marchenko, L. Journel, R. Guillemin, B. Pilette, T. Marin, and M. Simon, *J. Electron Spectrosc. Relat. Phenom.* **190**, 188 (2013).
- [36] M. O. Krause and J. H. Oliver, *J. Phys. Chem. Ref. Data* **8**, 329 (1979).
- [37] M. Breinig, M. H. Chen, G. E. Ice, F. Parente, B. Crasemann, and G. S. Brown, *Phys. Rev. A* **22**, 520 (1980).
- [38] G. C. King, M. Tronc, F. H. Read, and R. C. Bradford, *J. Phys. B* **10**, 2479 (1977).
- [39] L. Asplund, P. Kelfve, B. Blomster, H. Siegbahn, and K. Siegbahn, *Phys. Scr.* **16**, 268 (1977).
- [40] M. Žitnik, R. Püttner, G. Goldsztejn, K. Bučar, M. Kavčič, A. Mihelič, T. Marchenko, R. Guillemin, L. Journel, O. Travnikova *et al.*, *Phys. Rev. A* **93**, 021401 (2016).
- [41] A. Russek and W. Mehlhorn, *J. Phys. B* **19**, 911 (1986).
- [42] R. Püttner, P. Holzhey, M. Hrast, M. Žitnik, G. Goldsztejn, T. Marchenko, R. Guillemin, L. Journel, D. Koulentianos, O. Travnikova *et al.*, *Phys. Rev. A* **102**, 052832 (2020).
- [43] A. H. Clark, J. Imbao, R. Frahm, and M. Nachttegaal, *J. Synchrotron Radiat.* **27**, 551 (2020).
- [44] N. M. K. A. Vsevolod V. Balashov, Alexei N. Grum-Grzhimailo, *Polarization and Correlation Phenomena in Atomic Collisions: A Practical Theory Course*, Physics of Atoms and Molecules (Springer US, New York, 2000).
- [45] S. Fritzsche, *Comput. Phys. Commun.* **183**, 1525 (2012).
- [46] O. Zatsarinny, *Comput. Phys. Commun.* **98**, 235 (1996).
- [47] V. L. Sukhorukov, A. N. Hopersky, I. D. Petrov, V. A. Yavna, and V. F. Demekhin, *J. Phys.* **48**, 1677 (1987).
- [48] M. Deutsch, N. Maskil, and W. Drube, *Phys. Rev. A* **46**, 3963 (1992).